A CONSISTENT FINITE ELEMENT APPROACH TO LARGE EDDY SIMULATION

Frédéric Chalot[1]
Bernard Marquez[2]
Michel Ravachol[1]
Dassault Aviation, 92214 Saint-Cloud, France

Frédéric Ducros[1]
Franck Nicoud[1]
Thierry Poinsot[3]
CERFACS, 31057 Toulouse CEDEX, France

Abstract

This paper presents validation test cases of an LES solver based on an unstructured finite-element compressible Navier-Stokes code. After a short description of the industrial tool, we explain the incremental approach we have adopted in order to attain a reliable LES capability. Each step is illustrated by numerical examples and comparisons with experiments or theoretical results.

1. Introduction

Over the years, Computational Fluid Dynamics has become a true industrial tool, which, along with wind-tunnel and flight testing, contributes to the understanding of complex aerodynamics. Basic means of simulation, such as panel methods or potential flow, and inviscid calculations are nowadays key ingredients in the design process of an aircraft. As far as viscous effects are concerned, full Navier-Stokes computations gradually take over the classical boundary-layer approximation especially since the advent of practical turbulence models. Nevertheless, Reynolds Averaged Navier-Stokes, with turbulence models such as k-ε, remains the sole industrially viable approach yet. However, although Direct Numerical Simulation may still stay in the lab for a few more decades, Large Eddy Simulation (LES) might turn out to be the candidate compromise the industry is looking for. We may still be far away from computing sizable parts of an aircraft with LES, but it may reveal as a particularly useful tool to validate more advanced turbulence models.

[1] Research Scientist, Member AIAA
[2] Ph.D. Candidate
[3] Branch Head

The purpose of this work is to develop an LES capability in an industrial setting. The starting point is an existing finite-element code which has proven to be quite successful over a wide range of applications. Before diving into the selection and coding of subgrid models, and attempting ambitious computations, we wanted to make sure that the Navier-Stokes code at our disposal would satisfy the mere requirements for any decent LES calculation. In particular, we wanted convincing proofs that second order accuracy in space was sufficient and would yield valuable results.

The second section describes the initial industrial Navier-Stokes code, which is used on a daily basis for steady state computations. In the third section, we detail the numerical ingredients that were modified from that described in Section 2.

2. Description of the code

Dassault Aviation's Navier-Stokes code uses a finite element approach, based on a symmetric form of the equations written in terms of entropy variables. The advantages of this change of variables are numerous: in addition to the strong mathematical and numerical coherence they provide (dimensionally correct dot product, symmetric operators with positivity properties, efficient preconditioning), entropy variables yield further improvements over the usual conservation variables, in particular in the context of chemically reacting flows (see [5, 6]).

2.1. The symmetric Navier-Stokes equations

As a starting point, we consider the Euler and Navier-stokes equations written in conservative form:

$$\boldsymbol{U}_{,t} + \boldsymbol{F}^{\text{adv}}_{i,i} = \boldsymbol{F}^{\text{diff}}_{i,i} \tag{1}$$

where $\boldsymbol{U}$ is the vector of conservative variables; $\boldsymbol{F}_i^{\mathrm{adv}}$ and $\boldsymbol{F}_i^{\mathrm{diff}}$ are, respectively, the advective and the diffusive fluxes in the i^{th}-direction. Inferior commas denote partial differentiation and repeated indices indicate summation.

Equation (1) can be rewritten in quasi-linear form:

$$\boldsymbol{U}_{,t} + \boldsymbol{A}_i \boldsymbol{U}_{,i} = (\boldsymbol{K}_{ij} \boldsymbol{U}_{,j})_{,i} \tag{2}$$

where $\boldsymbol{A}_i = \boldsymbol{F}^{\mathrm{adv}}_{i,\boldsymbol{U}}$ is the i^{th} advective Jacobian matrix, and $\boldsymbol{K} = [\boldsymbol{K}_{ij}]$ is the diffusivity matrix, defined by $\boldsymbol{F}_i^{\mathrm{diff}} = \boldsymbol{K}_{ij}\boldsymbol{U}_{,j}$. The $\boldsymbol{A}_i$'s and $\boldsymbol{K}$ do not possess any particular property of symmetry or positiveness.

We now introduce a new set of variables,

$$\boldsymbol{V}^T = \frac{\partial \mathcal{H}}{\partial \boldsymbol{U}} \tag{3}$$

where $\mathcal{H}$ is the generalized entropy function given by

$$\mathcal{H} = \mathcal{H}(\boldsymbol{U}) = -\rho s \tag{4}$$

and s is the thermodynamic entropy per unit mass. Under the change of variables $\boldsymbol{U} \mapsto \boldsymbol{V}$, (2) becomes:

$$\widetilde{\boldsymbol{A}}_0 \boldsymbol{V}_{,t} + \widetilde{\boldsymbol{A}}_i \boldsymbol{V}_{,i} = (\widetilde{\boldsymbol{K}}_{ij} \boldsymbol{V}_{,j})_{,i} \tag{5}$$

where

$$\widetilde{\boldsymbol{A}}_0 = \boldsymbol{U}_{,\boldsymbol{V}} \tag{6}$$

$$\widetilde{\boldsymbol{A}}_i = \boldsymbol{A}_i \widetilde{\boldsymbol{A}}_0 \tag{7}$$

$$\widetilde{\boldsymbol{K}}_{ij} = \boldsymbol{K}_{ij} \widetilde{\boldsymbol{A}}_0. \tag{8}$$

The Riemannian metric tensor $\widetilde{\boldsymbol{A}}_0$ is symmetric positive-definite; the $\widetilde{\boldsymbol{A}}_i$'s are symmetric; and $\widetilde{\boldsymbol{K}} = [\widetilde{\boldsymbol{K}}_{ij}]$ is symmetric positive-semidefinite. In view of these properties, (5) is referred to as a symmetric advective-diffusive system.

For a general divariant gas, the vector of so-called (physical) entropy variables, $\boldsymbol{V}$, reads

$$\boldsymbol{V} = \frac{1}{T} \begin{Bmatrix} \mu - |\boldsymbol{u}|^2/2 \\ \boldsymbol{u} \\ -1 \end{Bmatrix} \tag{9}$$

where $\mu = e + pv - Ts$ is the chemical potential per unit mass; $v = 1/\rho$ is the specific volume. More complex equations of state are treated in [4].

Taking the dot product of (5) with the vector $\boldsymbol{V}$ yields the Clausius-Duhem inequality, which constitutes the basic nonlinear stability condition for the solutions of (5). This fundamental property is inherited by appropriately defined finite element methods, such as the one described in the next section.

2.2. The Galerkin/least-squares formulation

The Galerkin/least-squares (GLS) formulation introduced by Hughes and Johnson, is a full space-time finite element technique employing the discontinuous Galerkin method in time (see [18]). The least-squares operator ensures good stability characteristics while retaining a high level of accuracy. The local control of the solution in the vicinity of sharp gradients is further enhanced by the use of a nonlinear discontinuity-capturing operator.

We consider the time interval $I =]0, T[$, which we subdivide into N intervals $I_n =]t_n, t_{n+1}[$, $n = 0, \ldots, N-1$. Let $Q_n = \Omega \times I_n$ and $P_n = \Gamma \times I_n$ where Ω is the spatial domain of interest, and Γ is its boundary. In turn, the space-time "slab" Q_n is tiled by $(n_{\mathrm{el}})_n$ elements Q_n^e. Consequently, the Galerkin/least-squares variational problem can be stated as

> Within each Q_n, $n = 0, \ldots, N-1$, find $\boldsymbol{V}^h \in \mathcal{S}_n^h$ (trial function space), such that for all $\boldsymbol{W}^h \in \mathcal{V}_n^h$ (weighting function space), the following equation holds:

$$\begin{aligned}
&\int_{Q_n} \Big(-\boldsymbol{W}^h_{,t} \cdot \boldsymbol{U}(\boldsymbol{V}^h) - \boldsymbol{W}^h_{,i} \cdot \boldsymbol{F}_i^{\mathrm{adv}}(\boldsymbol{V}^h) \\
&\qquad + \boldsymbol{W}^h_{,i} \cdot \widetilde{\boldsymbol{K}}_{ij} \boldsymbol{V}^h_{,j} \Big)\, dQ \\
&+ \int_{\Omega} \Big(\boldsymbol{W}^h(t_{n+1}^-) \cdot \boldsymbol{U}\big(\boldsymbol{V}^h(t_{n+1}^-)\big) \\
&\qquad - \boldsymbol{W}^h(t_n^+) \cdot \boldsymbol{U}\big(\boldsymbol{V}^h(t_n^-)\big) \Big)\, d\Omega \\
&+ \sum_{e=1}^{(n_{\mathrm{el}})_n} \int_{Q_n^e} \Big(\mathcal{L}\boldsymbol{W}^h\Big) \cdot \boldsymbol{\tau} \Big(\mathcal{L}\boldsymbol{V}^h\Big)\, dQ \\
&+ \sum_{e=1}^{(n_{\mathrm{el}})_n} \int_{Q_n^e} \nu^h g^{ij} \boldsymbol{W}^h_{,i} \cdot \widetilde{\boldsymbol{A}}_0 \boldsymbol{V}^h_{,j}\, dQ \\
&= \int_{P_n} \boldsymbol{W}^h \cdot \Big(-\boldsymbol{F}_i^{\mathrm{adv}}(\boldsymbol{V}^h) \\
&\qquad + \boldsymbol{F}_i^{\mathrm{diff}}(\boldsymbol{V}^h) \Big) n_i\, dP.
\end{aligned} \tag{10}$$

The first and last integrals represent the Galerkin formulation written in integrated-by-parts form. The solution space consists of piecewise polynomials which are continuous in space, but are discontinuous across time slabs. Continuity in time is weakly enforced by the second integral in (10), which contributes to the jump condition between two contiguous slabs, with

$$\boldsymbol{Z}^h(t_n^{\pm}) = \lim_{\varepsilon \to 0^{\pm}} \boldsymbol{Z}^h(t_n + \varepsilon). \tag{11}$$

The third integral constitutes the least-squares operator where $\mathcal{L}$ is defined as

$$\mathcal{L} = \widetilde{\boldsymbol{A}}_0 \frac{\partial}{\partial t} + \widetilde{\boldsymbol{A}}_i \frac{\partial}{\partial x_i} - \frac{\partial}{\partial x_i}(\widetilde{\boldsymbol{K}}_{ij} \frac{\partial}{\partial x_j}). \tag{12}$$

$\boldsymbol{\tau}$ is a symmetric matrix for which definitions can be found in [18]. The fourth integral is the nonlinear discontinuity-capturing operator, which is designed to control oscillations about discontinuities, without upsetting higher-order accuracy in smooth regions. g^{ij} is the contravariant metric tensor defined by

$$[g^{ij}] = [\boldsymbol{\xi}_{,i} \cdot \boldsymbol{\xi}_{,j}]^{-1} \tag{13}$$

where $\boldsymbol{\xi} = \boldsymbol{\xi}(\boldsymbol{x})$ is the inverse isoparametric element mapping, and ν^h is a scalar-valued homogeneous function of the residual $\mathcal{L}\boldsymbol{V}^h$. The discontinuity capturing factor ν^h is is an extension of that introduced by Hughes, Mallet, and Shakib (see [18]). In the present work, the whole term is left out due to the regularity of the considered problems.

A key ingredient to the formulation is its consistency: the exact solution of (1) satisfies the variational formulation (10). This constitutes an essential property in order to attain higher-order spatial convergence.

2.3. Solution strategy

Convergence to steady state of the compressible Navier Stokes equations is achieved through a fully-implicit iterative time-marching procedure based on the GMRES algorithm (see [17]).

A low-storage extension based solely on residual evaluations was developed by Johan [13]. It reveals particularly adapted to parallel processing, where the linear solver often constitutes a painful bottleneck.

This algorithm has proven extremely efficient on many scalar or vector architectures (cf. [7, 14]). It is the basis on which all the LES developments we are going to describe, were built up.

2.4. Turbulence Models

Different turbulence models are available, including one-equation Spalart-Allmaras model, several versions of k-ε models with wall functions or low Reynolds number correction. The Navier-Stokes system and the additional turbulent equations are solved in a staggered manner which allows a great flexibility in the turbulence models. A robust and accurate technique was developed to enforce the positivity of the turbulence variables [6].

3. Towards LES

An intention of LES is to reduce the number of grid points required by DNS calculations. The mesh size can be further reduced by the use of unstructuredness. A few successful examples of the use of unstructured grid for LES can be found in [1, 10, 12].

The code described in the preceding section derives from its finite element structure, the capacity of treating any unstructured combination of tetrahedra and hexahedra. Any order of accuracy could be achieved with appropriate elements; in practice, linear elements are used which yield global second-order accuracy in space. This kind of accuracy proves to suffice for steady state calculations, but must still be critically evaluated in an LES framework.

3.1. Explicit versus implicit

In order to assess the space accuracy, any problem which may arise from a lack of time accuracy must be removed. Thus, we replaced the first-order constant-in-time scheme described in Section 2 with a classical fourth-order Runge-Kutta scheme (besides making the time-step global). In addition to being more accurate, this explicit approach alleviates the need of solving any linear system. In fact, no linear system solution can be guaranteed free of either numerical truncation error or incomplete convergence side effect. The use of a higher-order explicit scheme takes away all this potential problems at once, and enables the serene evaluation of the Galerkin/least-squares operator.

3.2. On the time-consistency of the Galerkin/least-squares operator

In equation (10), the Galerkin/least-squares operator reads:

$$\sum_{e=1}^{(n_{\mathrm{el}})_n} \int_{Q_n^e} \Big(\mathcal{L}\boldsymbol{W}^h\Big) \cdot \boldsymbol{\tau} \Big(\mathcal{L}\boldsymbol{V}^h\Big)\, dQ \tag{14}$$

This term is residual-based, which means that the exact solution of (1) is a solution of (10). This consistency property enforces higher-order accuracy in both space and time. For steady application, the term $\widetilde{\boldsymbol{A}}_0 \frac{\partial}{\partial t}$ is dropped out from the Navier-Stokes operator $\mathcal{L}$. In order to retain time accuracy, it is crucial that this term be reinstated (cf. [3]). In the framework of a Runge-Kutta scheme, we stress the fact that this time derivative must only be computed with final step solutions, and not with intermediate predictors; it is computed at the first Runge-Kutta step with the current solution and kept constant for all the remaining Runge-Kutta steps.

A modification of the intrinsic time-scale matrix $\boldsymbol{\tau}$ along the lines of [18] brings also additional time ingredients in the construction of the operator: the effect of the Galerkin/least-squares term is reduced with the time-step.

3.3. Numerical integration rule

All the integrals in (10) are numerically evaluated using Gaussian quadrature rules. As mentioned in Section 2.2, the time-dependent term and the Euler flux are integrated by parts, which preserves the conservation under reduced integration. However, although out-of-the-box finite element theory would recommend interpolating the solution variables, viz. the entropy variables $\boldsymbol{V}$, at the Gaussian integration points, it turns out that the interpolation of primitive variables $\boldsymbol{Q}^T = \{\rho, \boldsymbol{u}, p\}$ gives better results. This is especially true for phenomona driven by minute pressure variations.

4. <u>Numerical simulations</u>

The first simulation deals with homegeneous isotropic turbulence.

4.1. Homogeneous Isotropic Turbulence

The aim of the simulation of homegeneous isotropic turbulence at infinite Reynolds number is two-fold: first, check the ability of the stabilized formulation to recover the theoretical behavior for the enstrophy and the energy spectrum; second, calibrate the interaction between the stabilization and a subgrid scale model. All the simulations presented hereafter were performed using a 21^3 mesh. The initial condition was provided by CERFACS.

<u>Galerkin without subgrid model</u>

The first run was performed with Galerkin method, dropping out the least-squares term. No unstability problem may arise from the use of a centered scheme on this 3-D test case with periodic conditions in all three directions. As can be seen in Figures 2 and 3, the enstrophy grows unboundedly with time and the energy spectrum behaves as the theoretical k^2.

<u>Galerkin with subgrid model</u>

Still with a centered scheme, we added the simplest subgrid scale model available: the Smagorinsky model [19]. This model is assumed to work properly in the case of homegeneous isotropic turbulence. The analysis of the curves of enstrophy and turbulent kinetic energy shows that both quantities decay in $t^{-1.4}$ as theoretically expected. The spectra, presented in Figure 4, show that the energy is redistributed along the wave numbers and that a slope of $k^{-5/3}$ is recovered at the end of the computation.

A view of the pressure iso-surfaces at some point along the energy redistribution process, can be found in Figure 1. In this production phase, large structures can still be observed. Despite the relative coarseness of the mesh, the redistribution of energy toward the small scales takes place correctly.

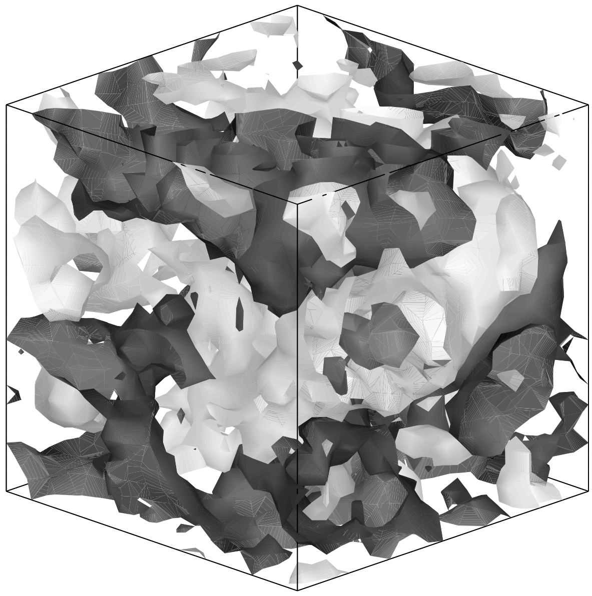

Figure 1. Homogeneous isotropic turbulence: pressure iso-surfaces.

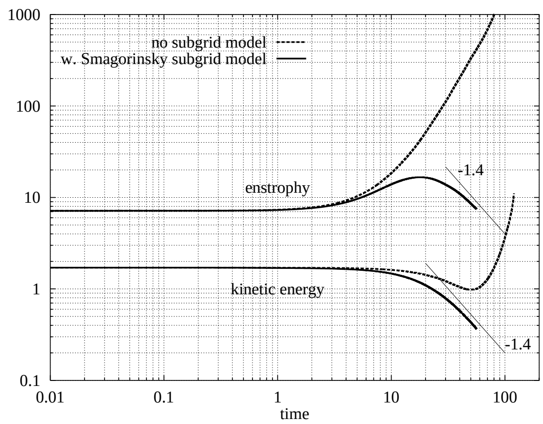

Figure 2. Homogeneous isotropic turbulence: kinetic energy and enstrophy time evolution for Galerkin w. and w/o subgrid model.

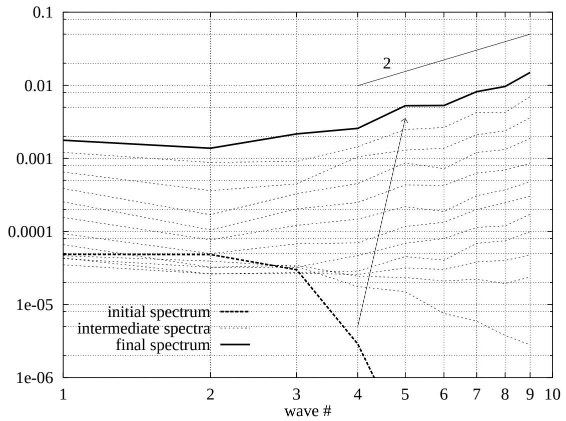

Figure 3. Homogeneous isotropic turbulence: energy spectrum for Galerkin w/o subgrid model.

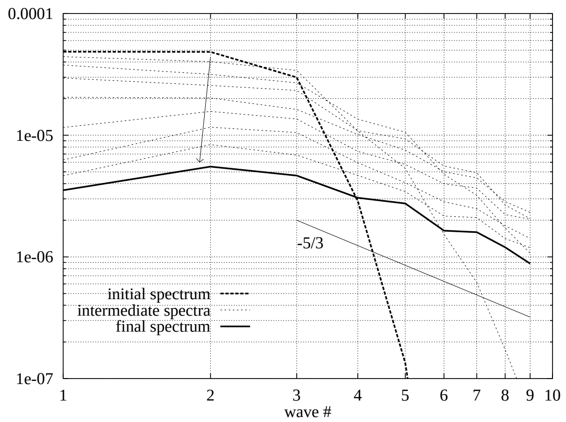

Figure 4. Homogeneous isotropic turbulence: energy spectrum for Galerkin w. subgrid model.

<u>Galerkin/least-squares</u>

We performed the same computations with the least-squares operator. Without subgrid scale model, the enstrophy grows but does not blow up (Figure 5). The energy spectrum shown in Figure 6, has a final slope proportional to k for the large wave numbers. Therefore, there is spurious dissipation; but the least-squares operator does not act as a subgrid scale model.

The simulation with the Smagorinsky model does not quite recover the theoretical slope for the energy spectrum, whilst the time decay of both the enstrophy and the kinetic energy agrees with the theory.

These results show an interaction between the stabilization and the subgrid model. One has to keep in mind that the computation was performed on a 21^3 grid. The effect of the number of grid points is being investigated, as well as the subgrid scale model: Smagorinsky replaced by a multi-scale model.

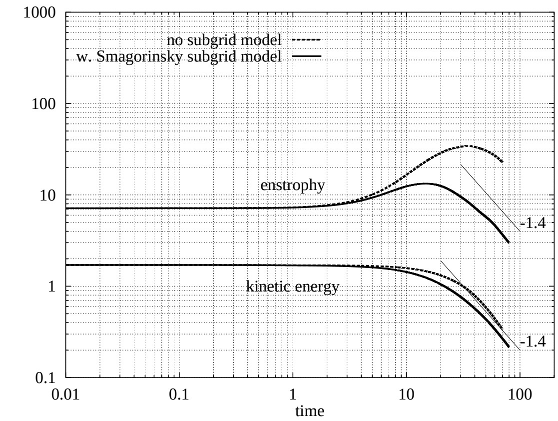

Figure 5. Homogeneous isotropic turbulence: kinetic energy and enstrophy time evolution for GLS w. and w/o subgrid model.

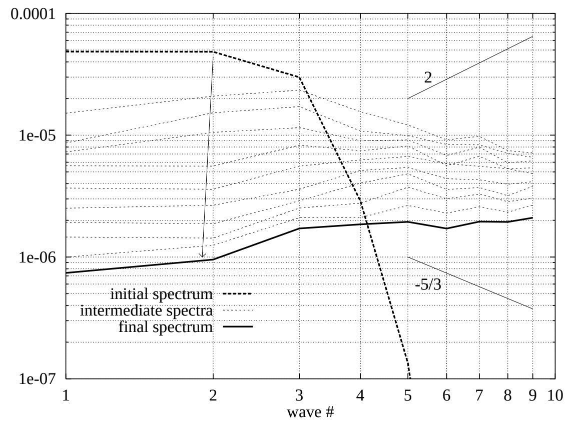

Figure 6. Homogeneous isotropic turbulence: energy spectrum for GLS w/o subgrid model.

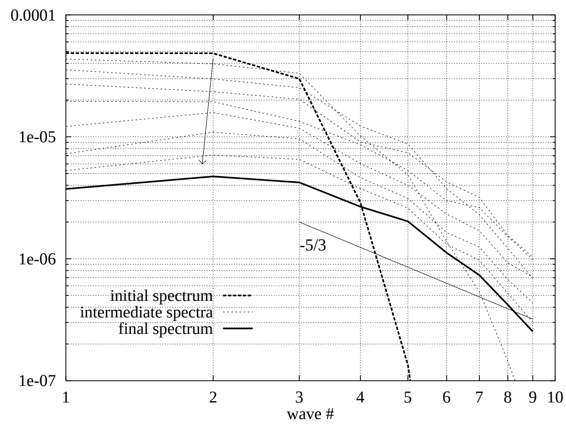

Figure 7. Homogeneous isotropic turbulence: energy spectrum for GLS w. subgrid model.

4.2. Periodic 2-D shear-layer

This test case consists in the calculation of an inviscid linear instability. We used different mesh sizes

(81×81 and 161×161) and point clustering. The results presented in Figures 8 and 9 were obtained on a uniform 161×161 mesh with Galerkin/least-squares without any subgrid model. The convective Mach number is 0.4 and the size of the domain is chosen such as to capture two vortices [11]. The initial velocity profile is an hyperbolic tangent on which we superimposed a white noise of intensity 10^{-3}. The initial temperature field is uniform. The amplification factor for the most amplified mode compares very well with the theory as shown in Figure 8. Figure 9 shows the two vortices before the pairing.

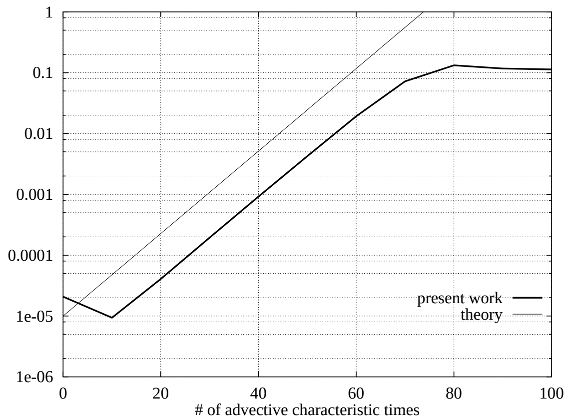

Figure 8. Periodic 2-D shear-layer: turbulent kinetic energy.

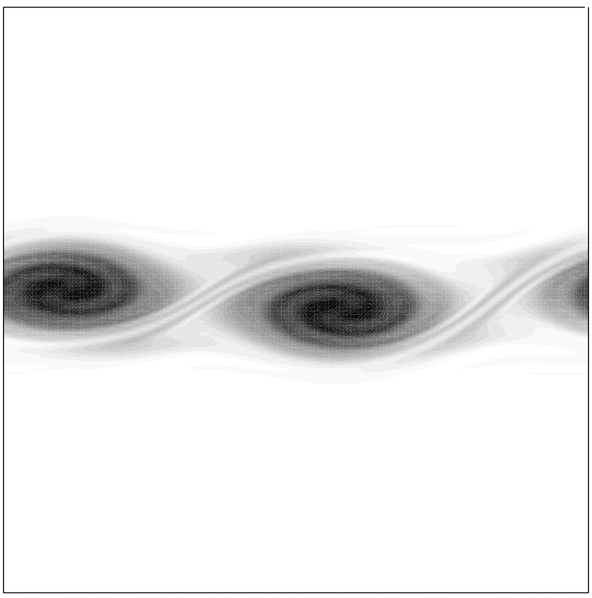

Figure 9. Periodic 2-D shear-layer: entropy contours.

4.3. Periodic 3-D shear-layer

The 3-D extension of the previous test case is currently being computed.

4.4. 2-D shear-layer

A subsonic/supersonic shear-layer with respective Mach numbers of 0.4 and 1.5 is computed next. Figure 10 shows the ability of Galerkin/least-squares to capture the spatial growth of an instability. The computation is being carried on to evaluate the statistics and compare the spreading rate with [15].

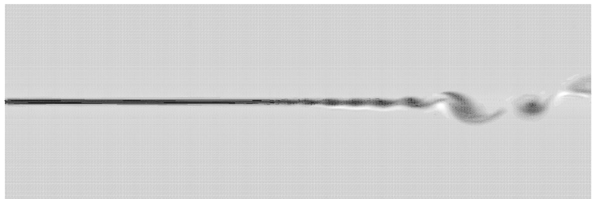

Figure 10. 2-D shear-layer: vorticity contours.

4.5. Periodic 2-D boundary-layer

A compressible laminar boundary-layer profile is used to initialize this test case. The Reynolds number based on the displacement thickness is 1000. The domain size is $22\delta_1 \times 50\delta_1$; it is meshed using 121×31 grid points. The streamwise periodicity is enforced through an appropriate source term which prevents the thickening of the boundary-layer. The wall is adiabatic, and pressure is imposed at the top wall.

Tollmien-Schlichting waves develop as can be seen in Figures 12 and 13. Linear stability results, such as the amplification factor of instabilities according to their wave lengths, corroborate the numerics (see Figure 11).

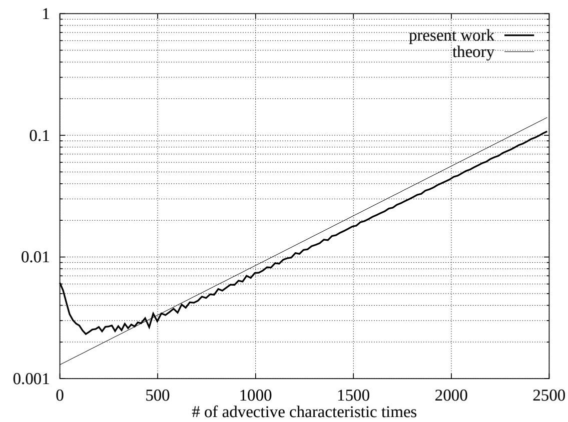

Figure 11. Periodic 2-D boundary-layer: turbulent kinetic energy.

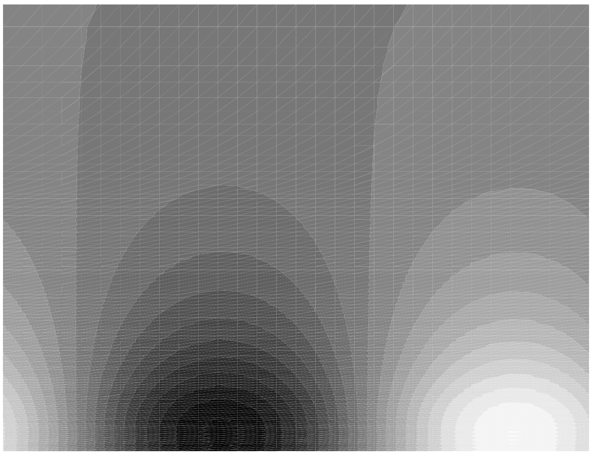

Figure 12. Periodic 2-D boundary-layer: pressure contours.

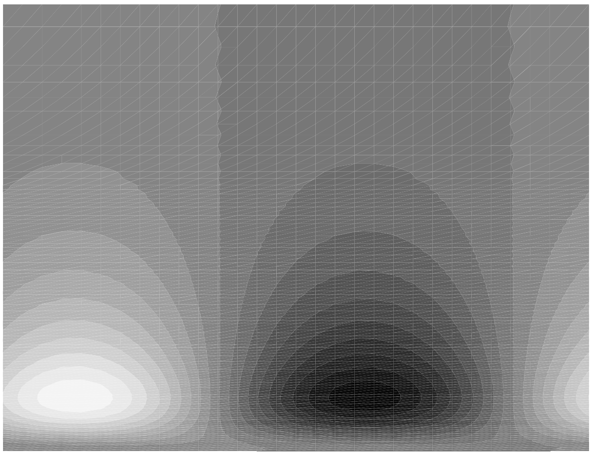

Figure 13. Periodic 2-D boundary-layer: vertical velocity contours.

5. Concluding remarks and perspective

This first set of cases shows the ability of an industrial code to be used for LES. More challenging computations shall be tackled in the near future.

Acknowledgements

The authors would like to thank Th. Poinsot, F. Nicoud, and C. Weber of CERFACS for giving us some insight on the realm of LES through numerous discussions.

B. Marquez is supported by a CIFRE fellowship from the French Ministries of Education and Research.

References

[1] F. Bastin, "Jet noise using large eddy simulation," *Annual Research Briefs*, Center for Turbulence Research, NASA Ames/Stanford University, pp 115–132, 1996.

[2] J.P. Bertoglio, *Simulation Numérique d'Ecoulements Turbulents*, Ecole de Printemps de Mécanique des Fluides Numérique, 1993.

[3] A.N. Brooks and T.J.R. Hughes, "Streamline Upwind Petrov Galerkin formulation for convection dominated flows with particular emphasis on the incompressible Navier-Stokes equations," *Computer Methods in Applied Mechanics and Engineering*, Vol. 32, pp 199–259, 1982.

[4] F. Chalot, T.J.R. Hughes, and F. Shakib, "Symmetrization of conservation laws with entropy for high-temperature hypersonic computations," *Computing Systems in Engineering*, Vol. 1, pp 495–521, 1990.

[5] F. Chalot and T.J.R. Hughes, "A consistent equilibrium chemistry algorithm for hypersonic flows," *Computer Methods in Applied Mechanics and Engineering*, Vol. 112, pp 25–40, 1994.

[6] F. Chalot, M. Mallet, and M. Ravachol, "A comprehensive finite element Navier-Stokes solver for low- and high-speed aircraft design," paper #94-0814, *AIAA 32nd Aerospace Sciences Meeting*, Reno, NV, January 10–13, 1994.

[7] F. Chalot, Q.V. Dinh, M. Mallet, A. Naïm, and M. Ravachol, "A multi-platform shared- or distributed-memory Navier-Stokes code," *Parallel CFD '97*, Manchester, UK, May 19–21, 1997.

[8] F. Ducros, *Simulations Directes et des Grandes Echelles de Couches Limites Compressibles*, Ph.D. Thesis, INPG, 1994.

[9] F. Ducros, P. Comte, and M. Lesieur, "Large eddy simulation of transition to turbulence in a boundary layer developing spatially over a flat plate," *Journal of Fluid Mechanics*, Vol. 326, pp 1–36, 1996.

[10] F. Ducros, F. Nicoud, and T. Schönfeld, "Large eddy simulations of compressible flows on hybrid meshes," *11th Symposium on Turbulent Shear Flows*, Grenoble, France, September 8–10, 1997.

[11] Y. Fouillet, *Contribution à l'Etude par Expérimentation Numérique des Ecoulements Cisaillés Libres: Effets de Compressibilité*, Ph.D. Thesis, INPG, 1991.

[12] K. Jansen, "Preliminary large-eddy simulations of flow over a NACA 4412 airfoil using unstructured grids," *Annual Research Briefs*, Center for Turbulence Research, NASA Ames/Stanford University, pp 61–72, 1995.

[13] Z. Johan, T.J.R. Hughes, and F. Shakib, "A globally convergent matrix-free algorithm for implicit time-marching schemes arising in finite element analysis in fluids," *Computer Methods in Applied Mechanics and Engineering*, Vol. 87, pp 281–304, 1991.

[14] Z. Johan, *Data Parallel Finite Element Techniques for Large-scale Computational Fluid Dynamics*, Ph.D. Thesis, Stanford University, 1992.

[15] D. Papamoschou and A. Roshko, "The compressible turbulent shear layer: an experimental study," *Journal of Fluid Mechanics*, Vol. 197, pp 453–477, 1988.

[16] T. Poinsot and S.K. Lele, "Boundary conditions for direct simulations of compressible viscous reacting flows," *Journal of Computational Physics*, Vol. 101, pp 104–129, 1992.

[17] F. Shakib, T.J.R. Hughes, and Z. Johan, "A multi-element group preconditioned GMRES algorithm for nonsymmetric systems arising in finite element analysis," *Computer Methods in Applied Mechanics and Engineering*, Vol. 75, pp 415–456, 1989.

[18] F. Shakib, T.J.R. Hughes, and Z. Johan, "A new finite element formulation for computational fluid dynamics: X. The compressible Euler and Navier-Stokes equations," *Computer Methods in Applied Mechanics and Engineering*, Vol. 89, pp 141–219, 1991.

[19] J. Smagorinsky, "General circulation experiments with the primitive equations, I: The basis experiment," *Monthly Weather Review*, Vol. 91, pp 99–163, 1963.